NEW DIFFRACTION DATA

Tetragonal–cubic phase transition in RbGaSi$_2$O$_6$ synthetic leucite analogue

Anthony Martin Thomas Bell and Francis Sweeney

Materials and Engineering Research Institute, Sheffield Hallam University, Sheffield, UK

Abstract: The leucite group structures are tetrahedrally coordinated silicate framework structures with some of the silicate framework cations partially replaced by divalent or trivalent cations. These structures have general formulae A_2BSi$_5$O$_{12}$ and ACSi$_2$O$_6$, where A is a monovalent alkali metal cation, B is a divalent cation, and C is a trivalent cation. These leucites can have crystal structures in several different space groups, dependent on stoichiometry, synthesis conditions, and temperature. Phase transitions are known for temperature changes. This paper reports a high-temperature X-ray powder diffraction study on RbGaSi$_2$O$_6$, which shows a phase transition from $I4_1/a$ tetragonal to Ia-3d bar on top of 3 cubic on heating from room temperature to 733 K. On cooling to room temperature, the crystal structure reverts to $I4_1/a$ tetragonal.

[doi:10.1017/S0885715625101097]

I. INTRODUCTION

Synthetic anhydrous analogues of the silicate framework minerals leucite (end-member KAlSi$_2$O$_6$) and pollucite (end-member CsAlSi$_2$O$_6$) can be prepared with the general formulae A_2BSi$_5$O$_{12}$ and ACSi$_2$O$_6$, where A is a monovalent alkali metal cation, B is a divalent cation, and C is a trivalent cation (Torres-Martinez and West, 1984, 1986, 1989; Torres-Martinez et al., 1984). These structures all have the same topology, with B and C cations partially substituting onto tetrahedrally coordinated sites (T-sites) in the silicate framework and charge-balancing A cations sitting in the extra-framework channels. The A cations can be replaced by ion exchange. Cs-containing silicate framework minerals are of potential technological interest as storage media for radioactive Cs from nuclear waste (Gatta et al., 2008). A review paper on leucite crystal structures has been published (Bell, 2025).

X-ray and neutron powder diffraction have been used to determine and refine the ambient temperature crystal structures of leucite analogues with the general formulae A_2BSi$_5$O$_{12}$ and ACSi$_2$O$_6$. Crystal structures have been refined in the *Ia-3d 3 with bar above* cubic and $I4_1/a$ tetragonal space groups (A = K, Rb, Cs; B = Mg, Mn, Co, Ni, Cu, Zn; C = Fe^{3+}, Ga; Bell et al., 1994a, 2010; Bell and Henderson, 1994a, 1994b, 2018, 2020; Bell and Stone, 2021). These structures all have *disordered* T-site cations and have A cation sites fully occupied with either K, Rb, or Cs. CsGaSi$_2$O$_6$ also has a disordered T-site structure in the space group $I\bar{4}3d$ (Bell and Stone, 2021). Crystal structures have also been refined

at ambient temperature for *P*2$_1$/*c* monoclinic crystal structures of leucite analogues with the general formulae A_2BSi$_5$O$_{12}$ (A = K; B = Mg, Fe^{2+}, Co, Zn; Bell et al., 1994a; Bell and Henderson, 2018) and also for *Pbca* orthorhombic (A = Rb; B = Mg, Mn, Ni, Cd; Bell and Henderson, 1996, 2009, 2016) and (A = Cs; B = Mg, Mn, Co, Ni, Cu, Zn, Cd; Bell et al., 1994b; 2010; Bell and Henderson, 1996, 2009). These structures all have *ordered* T-site cations and have A cation sites fully occupied with either K, Rb, or Cs. RbCsX^{2+}Si$_5$O$_{12}$ (X = Mg, Ni, Cd) leucite analogues, with two different extra-framework alkali metal cations, all have the *Pbca* structure with ordered T-site cations (Bell and Henderson, 2019). For X = Ni and Cd, these structures have disordered extra-framework cations, but for X = Mg, there is partial ordering of the extra-framework cations. Cs$_2X^{2+}$Si$_5$O$_{12}$ (X = Cd, Cu, Zn) all retain the cation-ordered *Pbca* orthorhombic structure below 10 K (Bell, 2021).

KAlSi$_2$O$_6$ (leucite), Rb-substituted leucite RbAlSi$_2$O$_6$, Cs-substituted leucite CsAlSi$_2$O$_6$, and KFeSi$_2$O$_6$ all have the $I4_1/a$ *disordered* T-site cation structure at room temperature, but all undergo high-temperature phase transitions to the pollucite $Ia\bar{3}d$ *disordered* T-site cation structure (Palmer et al., 1997). KGaSi$_2$O$_6$ similarly undergoes a phase transition from $I4_1/a$ to $Ia\bar{3}d$ over the temperature range from 673 to 970 K (Bell and Henderson, 2020).

Cs$_2$ZnSi$_5$O$_{12}$ undergoes a reversible phase transition from *Pbca* (*ordered* T-site cation structure) to $Pa\bar{3}$ (*disordered* T-site cation structure) on heating to 566 K (Bell and Henderson, 2012). Rb$_2$CoSi$_5$O$_{12}$ also has a phase transition from *Pbca* to $Pa\bar{3}$ on heating to 457 K (Bell, 2023). K$_2$MgSi$_5$O$_{12}$ and K$_2$ZnSi$_5$O$_{12}$ both undergo phase transitions from *P*2$_1$/*c* to *Pbca* on heating to 622 K (K$_2$MgSi$_5$O$_{12}$; Redfern and Henderson, 1996) and over the temperature range from 843 to 868 K (K$_2$ZnSi$_5$O$_{12}$; Bell et al., 2021).

Corresponding author: Anthony Martin Thomas Bell; Email: Anthony.Bell@shu.ac.uk

In this paper, a high-temperature phase transition in the synthetic leucite analogue with stoichiometry of $RbGaSi_2O_6$ is reported.

II. EXPERIMENTAL

A. Sample synthesis and ambient temperature X-ray powder diffraction

The $RbGaSi_2O_6$ synthetic leucite analogue was prepared by heating a stoichiometric mixture of Rb_2CO_3, SiO_2, and Ga_2O_3 to 1473 K; this produced a white powdered sample. Before mixing, the starting materials SiO_2 and Ga_2O_3 were dried overnight at 383 K and Rb_2CO_3 was stored in a nitrogen filled glove box. Ambient temperature X-ray powder diffraction and Rietveld refinement (Rietveld, 1969) showed the presence of an $RbGaSi_2O_6$ phase that was isostructural with $KGaSi_2O_6$ and $KAlSi_2O_6$. Ga_2O_3 was present as an impurity phase. For full details, see Bell and Stone (2021).

B. High-temperature X-ray powder diffraction data collection

The $RbGaSi_2O_6$ sample was loaded on a Pt flat plate sample holder in an Anton–Paar HTK1200N high-temperature stage, which was mounted on a PANalytical X'Pert Pro MPD using Cu $K\alpha$ X-rays, with a nickel β-filter and a 3.3473 °2θ wide 255 channel PIXCEL-1D area detector. An initial ambient temperature XRD scan was done over the range from 10 to 120 °2θ; this confirmed the presence of $I4_1/a$ tetragonal $RbGaSi_2O_6$ and Ga_2O_3 impurity phase. High-temperature XRD data (run 1) were collected over the range from 25 to 27 °2θ with a step width of 0.0131 °2θ using Data Collector 5.5a (PANalytical, 2017a); the beam size was defined with a 10-mm mask, fixed antiscatter (¼ °) and divergence (⅛ °) slits. These data showed the tetragonal (004) and (400) Bragg reflections for $RbGaSi_2O_6$ at room temperature. XRD datasets were collected at 298 K and then in 50 K temperature steps from 323 to 973 K. The HTK1200N high-temperature stage has a stage mover, which adjusts the sample height to keep the centre of the sample in the X-ray beam with changes in temperature.

More XRD data (run 2) were then collected using the X'Pert over the range from 15 to 100 °2θ; 30-minute scans were collected at 298 K, 623 K, and in 10 K steps from 673 to 823 K. A 10-hour scan was then done at 873 K to get Rietveld quality XRD data before a final 30-minute scan was done after cooling to 298 K.

No smoothing or α_2 stripping was done on any of these data. The diffractometer was calibrated with an external NIST 640e silicon standard.

C. Scanning electron microscopy analysis

An FEI Quanta 650 scanning electron microscope (SEM) is equipped with an Oxford Instruments energy dispersive spectroscopy (EDS) system that incorporates an XMax 80-mm^2 detector capable of detecting all elements from Be to Pu. This system was utilized to perform chemical analysis on an $RbGaSi_2O_6$ sample. Electron micrographs and EDS data were recorded using an electron beam energy of 20 keV and a beam current of 0.31 nA.

Prior to the SEM investigation, the sample was carbon-coated using an EMITech K950X carbon coater for a duration of 800 milliseconds, producing a thin electron transparent coating with a thickness of <10 nm.

D. X-ray powder diffraction data analysis

The initial run 1 XRD data were collected over the range from 25 to 27 °2θ. These data showed the tetragonal (004) and (400) Bragg reflections for $RbGaSi_2O_6$ at room temperature. On heating, these two Bragg reflections get closer together. By 773 K, these two reflections have merged into a single peak, suggesting a transition to a cubic structure (see Figure 1).
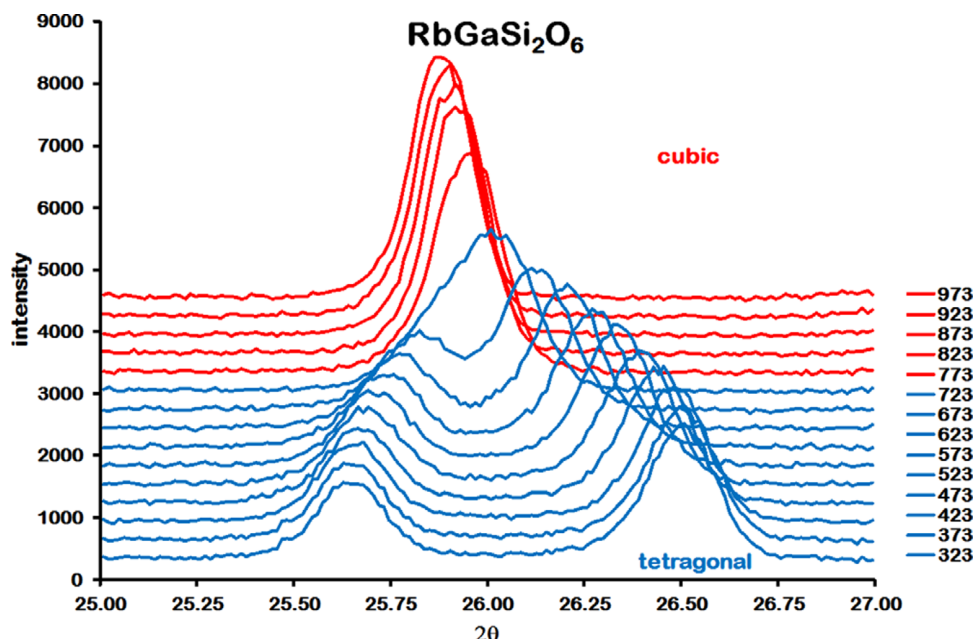

Figure 1. High-temperature XRD data for $RbGaSi_2O_6$ over the range of 25–27°2θ, measured from 323 to 973 K.

The subsequent run 2 XRD data were collected as 30-minute scans over the range from 15 to 100 °2θ at 298 K, 623 K, and in 10 K steps from 673 to 823 K before a 10-hour scan at 873 K.

These run 2 powder diffraction data were analyzed using HighScore Plus 4.7 (PANalytical, 2017b) and the ICDD Powder Diffraction File (Kabekkodu et al., 2024). Analysis of the 298 K powder diffraction data for $RbGaSi_2O_6$ showed that this sample consisted of two phases. The main phase was $I4_1/a$ tetragonal $RbGaSi_2O_6$ PDF# 00-037-0350 with $C2/m$ monoclinic Ga_2O_3 PDF# 00-043-1012 as an impurity phase. Rietveld refinements were done using FULLPROF (Rodríguez-Carvajal, 1993) for

XRD data collected up to 823 K. GSAS-II (Toby and Von Dreele, 2013) was used for Rietveld refinements on the 873 K data. Backgrounds were fitted by linear interpolation between a set of background points with refinable heights. The Thompson–Cox–Hastings pseudo-Voigt function (van Laar and Yelon, 1984), convoluted with asymmetry due to axial divergence (Finger et al., 1994), was used to model the profile shape.

The crystal structure of $RbGaSi_2O_6$ was refined using the $I4_1/a$ structure of $RbGaSi_2O_6$ (Bell and Stone, 2021) as the starting model. In this crystal structure, all atoms were located on the $I4_1/a$ 16f Wyckoff general position. There is one 16f position for Rb, three 16f positions for T-sites (with
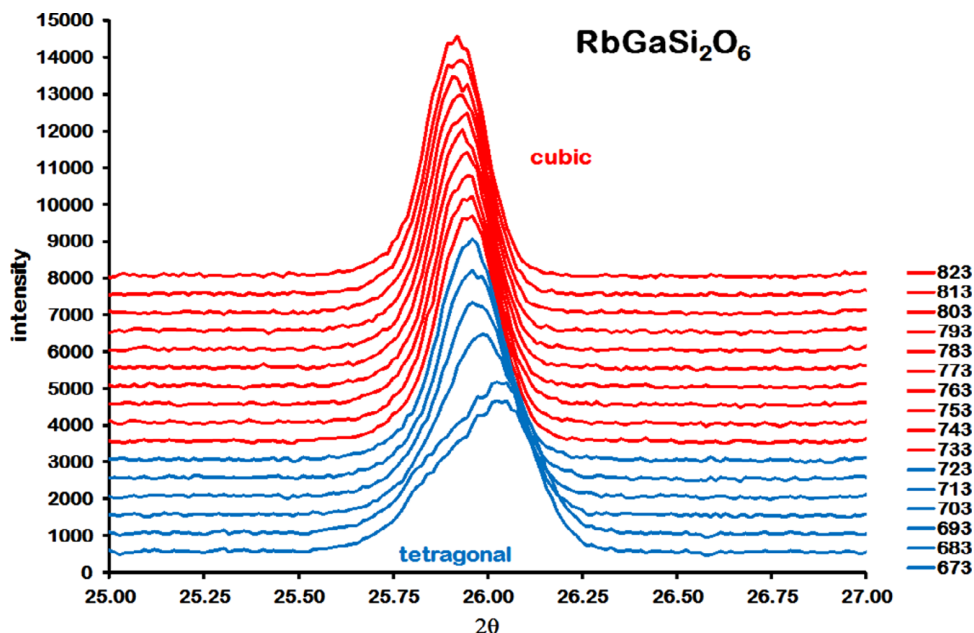

Figure 2. High-temperature XRD data for $RbGaSi_2O_6$ over the range of 25–27°2θ, measured from 673 to 823 K.
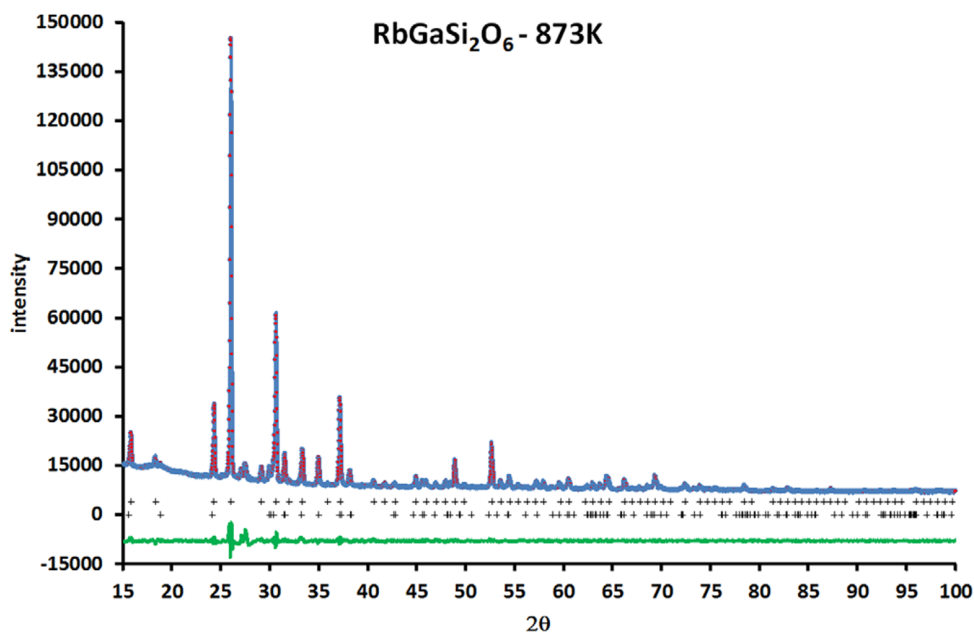

Figure 3. Rietveld difference plot for $RbGaSi_2O_6$ from data collected at 873 K. The red circles represent the observed data points, the blue line represents the calculated data points, and the green line represents the difference curve. The upper line of black crosses represents the positions of Bragg reflections for $RbGaSi_2O_6$, whereas the lower line of black crosses represents the positions of Bragg reflections for Ga_2O_3 impurity. R-factors for this refinement were $R_p = 2.044\%$, $R_{wp} = 3.282\%$, $R_{exp} = 1.013\%$, and $\chi^2 = 3.24$.

disordered occupancies of one-third Ga and two-thirds Si, T-site occupancies were not refined), and six 16f positions for O. The isotropic temperature factors of the T-site atoms Si and Ga were constrained to be the same on each T-site but were allowed to vary between different T-sites. All isotropic temperature factors for the six O sites were constrained to have the same value. The T–O interatomic distances were soft constrained to be 1.68 ± 0.02 Å (average bond distance for tetrahedral Si–O and Ga–O), assuming complete T-site disorder (1/3Ga:2/3Si on each T-site), as it was not possible to refine chemically sensible T-site occupancies. Rietveld refinements in non-cubic leucite structures without soft interatomic distance constraints tend to give unrealistic interatomic T–O distances. The crystal structure of Ga_2O_3
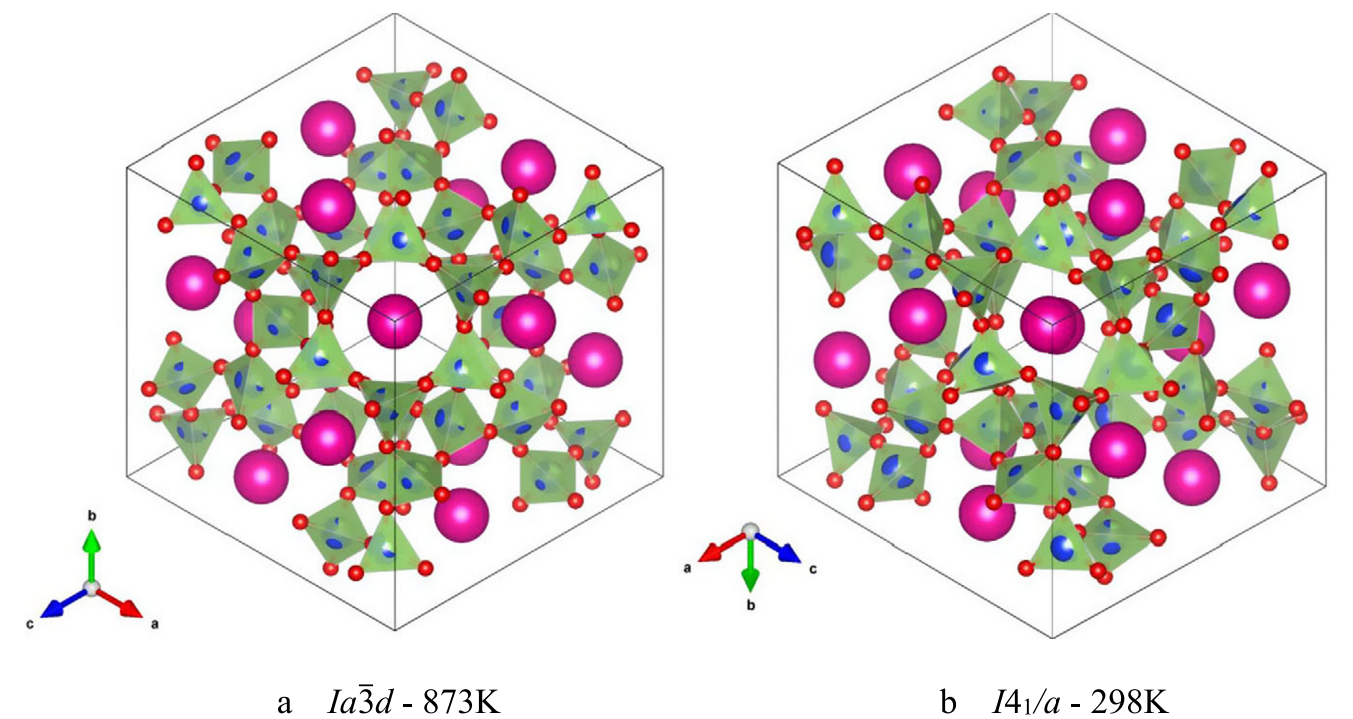

a $Ia\bar{3}d$ - 873K   b $I4_1/a$ - 298K

Figure 4.   VESTA structure plots for $RbGaSi_2O_6$. Extra-framework Rb^+ cations are shown in pink, disordered $(Si/Ga)O_4$ tetrahedra in light green, and O^{2-} anions in red. Panel (a) shows the $Ia\bar{3}d$ cubic 873 K crystal structure, viewed down [111], showing the channel for extra-framework cations. Panel (b) shows the $I4_1/a$ tetragonal 298 K crystal structure, viewed down [1-11], showing the channel for extra-framework cations (Bell and Stone, 2021).

TABLE I.   Variation of $RbGaSi_2O_6$ lattice parameters and phase proportions on heating.

	Temp (K)	a(Å)	c(Å)	V(Å³)	c/a	wt.% $RbGaSi_2O_6$	wt.% Ga_2O_3
	298	13.3752(6)	13.8040(6)	2,469.47(19)	1.03206(9)	87(1)	13.1(3)
	623	13.5573(5)	13.7145(6)	2,520.71(17)	1.01160(8)	88(1)	11.7(2)
	673	13.5971(5)	13.6928(5)	2,531.55(17)	1.00704(7)	88(1)	11.7(2)
	683	13.6044(5)	13.6870(5)	2,533.20(16)	1.00607(7)	88(1)	12.1(2)
	693	13.6130(5)	13.6818(5)	2,535.40(15)	1.00505(7)	88(1)	12.2(2)
	703	13.6212(4)	13.6789(5)	2,537.92(15)	1.00424(6)	88(1)	12.0(2)
	713	13.6289(4)	13.6763(5)	2,540.34(14)	1.00348(6)	88(1)	12.1(2)
	723	13.6325(4)	13.6748(5)	2,541.40(14)	1.00310(6)	88(1)	12.3(2)
	733	13.6483(3)		2,542.33(9)		87(1)	13.0(2)
	743	13.6514(3)		2,544.11(9)		87.3(9)	12.7(3)
	753	13.6534(3)		2,545.23(9)		87.1(9)	12.9(2)
	763	13.6550(3)		2,546.10(8)		87(1)	12.8(2)
	773	13.6566(3)		2,547.00(8)		87.3(9)	12.7(2)
	783	13.6587(3)		2,548.15(8)		87.4(9)	12.7(2)
	793	13.6601(3)		2,548.96(9)		87(1)	13.0(2)
	803	13.6625(3)		2,550.28(8)		86.8(9)	13.2(2)
	813	13.6632(3)		2,550.67(8)		87.1(9)	12.9(2)
	823	13.6641(3)		2,551.20(8)		87.3(9)	12.7(2)
	873	13.6731(3)		2,556.22(18)		87.4(1)	12.6(1)
X	298	13.3739(6)	13.8036(6)	2,468.93(19)		87(1)	12.7(3)
XX	298	13.3703(2)	13.7983(2)	2,466.66(7)		88.2(6)	11.8(1)

298–723 K: I41/a tetragonal; 733–873 K: Ia$\bar{3}$d cubic. "X" denotes data collected in the furnace after heating, and "XX" denotes ambient-temperature data not measured in the furnace (Bell and Stone, 2021).

(da Silva et al., 2012) was used to fit the impurity phase; only lattice parameters were refined.

The refined structural parameters were used as a starting model for the 623 K data; subsequent refinements were done with the refined parameters used as a starting model for the next temperature up. As the temperature increased, the a and c lattice parameters moved closer together. At 733 K, the a and c lattice parameters were so close that it was possible to refine the crystal structure for $RbGaSi_2O_6$ with an $Ia\bar{3}d$ cubic structure that was isostructural with pollucite ($CsAlSi_2O_6$). In this cubic structure, Rb replaced Cs on the extra-framework cation site and Ga replaced Al on the disordered T-site. This cubic structure was retained up to 873 K. Figure 2 shows the run 2

XRD data over the range from 25 to 27 °2θ heating from 673 to 823 K. This shows how a closely overlapped double peak for the tetragonal (004) and (400) Bragg reflections merge to form a single cubic (400) Bragg reflection at 733 K. Figure 3 shows a Rietveld difference plot for $RbGaSi_2O_6$ at 873 K; this difference plot shows Bragg reflections for cubic $RbGaSi_2O_6$ and Ga_2O_3 impurity. Note that there are also two weak unassigned Bragg reflections at 27.15 and 27.55 °2θ in the 873 K difference plot.

VESTA (Momma and Izumi, 2011) was used to plot crystal structures. Figure 4a,b, respectively, shows the crystal structure plots for $RbGaSi_2O_6$ at 873 and 298 K (Bell and Stone, 2021).

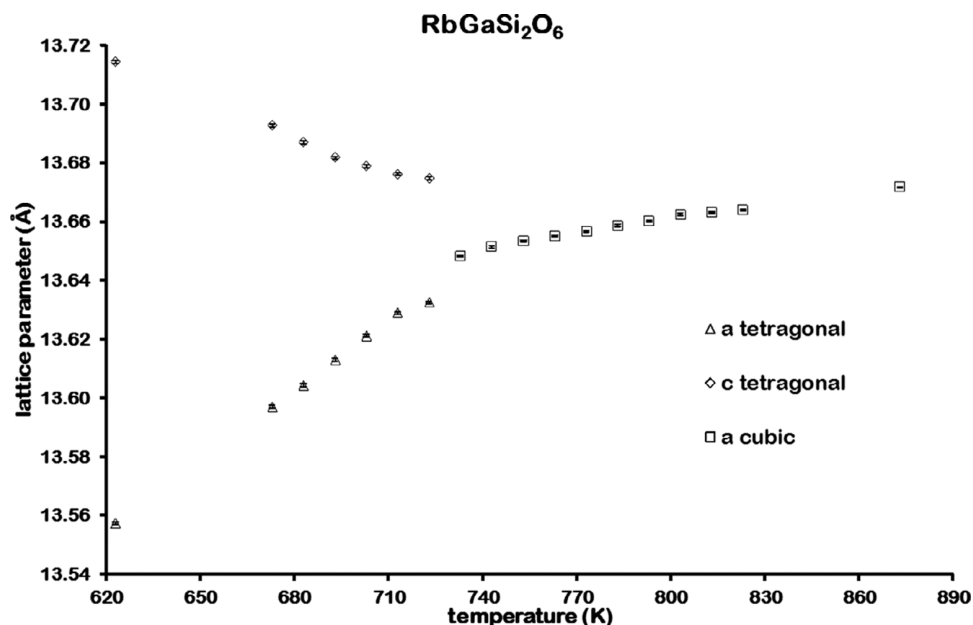Figure 5.   Variation of lattice parameters for $RbGaSi_2O_6$ from 623 to 873 K.

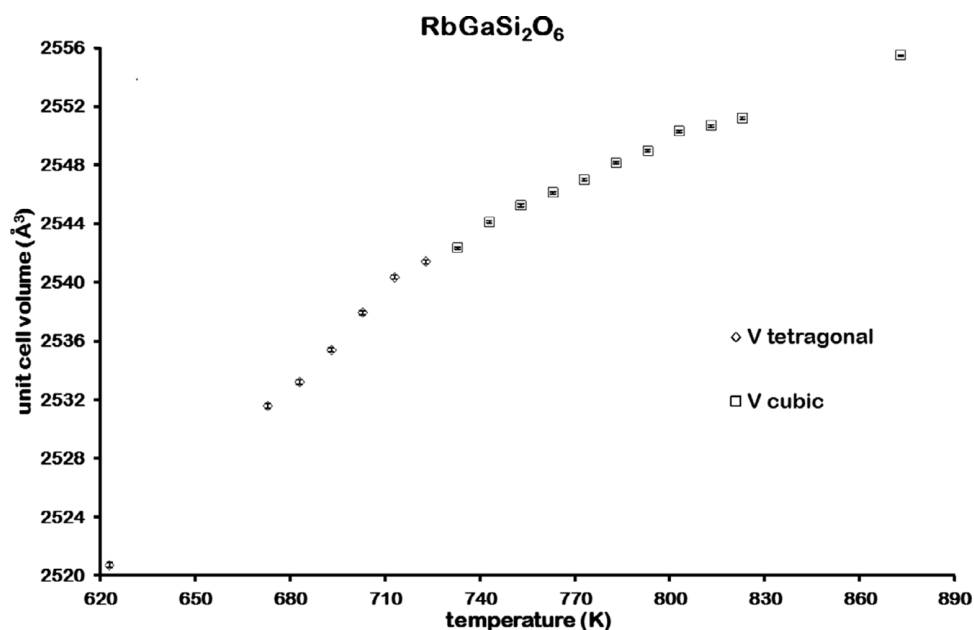Figure 6.   Variation of unit cell volume for $RbGaSi_2O_6$ from 623 to 873 K.

TABLE II. Refined cubic coordinates for RbGaSi$_2$O$_6$ $Ia\overline{3}d$ at 873 K.

Atom	Wyckoff	x	y	z	Occupancy	U_{iso}(Å^2)
Rb	16b	0.125	0.125	0.125	1.0000	0.1008(13)
Ga	48g	0.66337(8)	0.58663(8)	0.125	0.3333	0.0309(8)
Si	48g	0.66337(8)	0.58663(8)	0.125	0.6667	0.0309(8)
O	96h	0.10384(21)	0.13692(21)	0.71767(12)	1.0000	0.0745(20)

III. RESULTS AND DISCUSSION

Crystal structures have been refined for the RbGaSi$_2$O$_6$ leucite analogue from X-ray powder diffraction data over the temperature range from 298 to 873 K. All refined structures have disordered T-site cations. RbGaSi$_2$O$_6$ is isostructural with $I4_1/a$ tetragonal leucite (KAlSi$_2$O$_6$; Mazzi et al., 1976) from 298 to 723 K. At 733 K, there is a phase transition, and the crystal structure is then isostructural with $Ia\overline{3}d$ cubic pollucite (CsAlSi$_2$O$_6$; Yanase et al., 1997). Table I shows how the refined lattice parameters for RbGaSi$_2$O$_6$ vary with temperature, and Figures 5 and 6 show how the lattice parameters and unit cell volume for RbGaSi$_2$O$_6$ vary with temperature. Table II shows the refined coordinates, and Table III shows the refined interatomic distances and angles for RbGaSi$_2$O$_6$ at 873 K.

Figure 6 shows how the unit cell volume for RbGaSi$_2$O$_6$ varies with temperature; there is no step change in unit cell volume at the phase transition temperature at 733 K. This suggests that RbGaSi$_2$O$_6$ has a second-order $I4_1/a$ tetragonal to $Ia\overline{3}d$ cubic phase transition. KGaSi$_2$O$_6$ also has an $I4_1/a$ tetragonal to $Ia\overline{3}d$ cubic phase transition (Bell and Henderson, 2020). However, this transition is different from that of RbGaSi$_2$O$_6$ in that there is a two-phase region in this transition. Bragg reflections for both cubic and tetragonal KGaSi$_2$O$_6$ are present over the temperature range from 673 to 970 K; no similar two-phase region is observed for RbGaSi$_2$O$_6$. There is also a step change in unit cell volume from tetragonal to cubic for KGaSi$_2$O$_6$, suggesting a first-order phase transition.

The equations of Carpenter (Carpenter et al., 1998) have been used to determine the spontaneous strain parameters for RbGaSi$_2$O$_6$ and KGaSi$_2$O$_6$ below the tetragonal to cubic phase transition temperatures. Figure 7 shows the variation of the spontaneous strain, and Figure 8 shows the variation of the e_{11} and e_{33} strain parameters for RbGaSi$_2$O$_6$ and KGaSi$_2$O$_6$. These figures show that the magnitudes of the strain parameters are greater for KGaSi$_2$O$_6$ compared with RbGaSi$_2$O$_6$. This may be due to the smaller K$^+$ extra-framework cation causing a greater degree of framework collapse (Taylor and Henderson, 1968) compared with the larger Rb$^+$ extra-framework cation. Consequently, the tetragonal

TABLE III. Refined distances and angles for RbGaSi$_2$O$_6$ $Ia\overline{3}d$ at 873 K.

Atom pairs	Distance(Å)	Distance(Å)
Rb–Ox6	3.5052(29)	3.3797(29)
T–Ox2	1.6515(16)	1.6556(17)

Atom triplets	Angle(°)	Angle(°)
O–T–O x2	114.49(17)	110.46(20)
O–T–O	106.89(20)	100.22(17)
T–O–T	141.52(17)	

"T" denotes the disordered Ga/Si site. Tetrahedral angle variance [σ^2, deg^2] for $Ia\overline{3}d$ RbGaSi$_2$O$_6$ at 873 K = 28.92. $\sigma^2 = \Sigma(\theta - 109.47)^2/5$ (Robinson et al., 1971), where θ is the O–T–O tetrahedral angle.

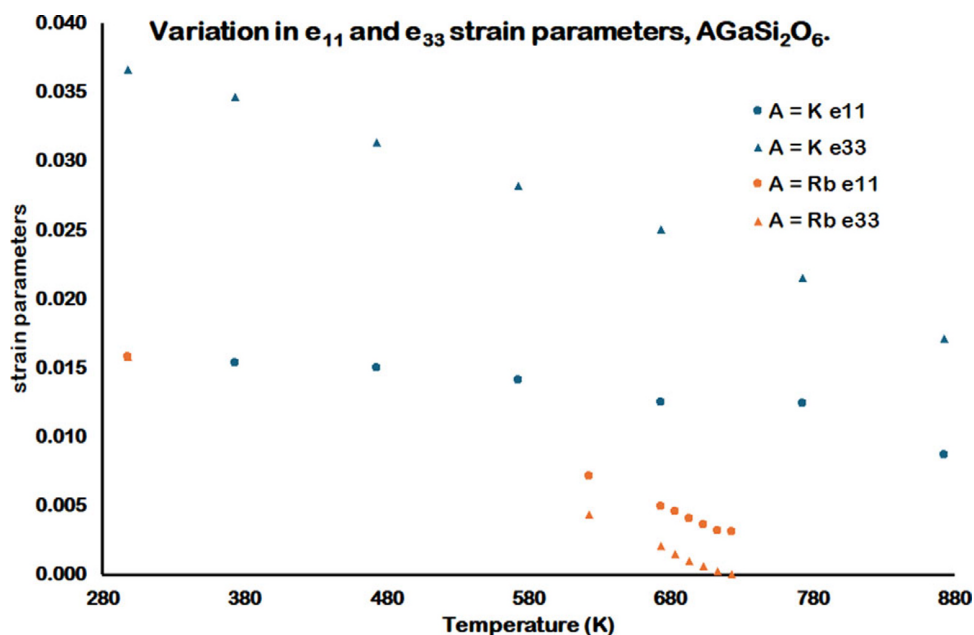Figure 7. Variation spontaneous strain parameters for tetragonal AGaSi$_2$O$_6$ (A = K, Rb) from 298 to 873 K.

Figure 8. Variation in e_{11} and e_{33} strain parameters for tetragonal $AGaSi_2O_6$ (A = K, Rb) from 298 to 873 K. Note that the A = K e_{33} and the A = Rb e_{11} and e_{33} strain parameters at 298 K cannot be resolved in this figure, as these parameters have similar values.

crystal structure for $KGaSi_2O_6$ would show a greater degree of strain compared with $RbGaSi_2O_6$.

Ga_2O_3 is present as an impurity phase at all temperatures. Table I shows that the phase proportion of $RbGaSi_2O_6$ is constant within error limits over the temperature range. This indicates that there is no further reaction of impurity Ga_2O_3 over the temperature range. However, Table I shows that the Ga_2O_3 is present as an impurity phase at approximately 12 wt.%. Rietveld refinements were done using the $I4_1/a$ tetragonal (leucite) and $Ia\bar{3}d$ cubic (pollucite) crystal structures as starting models; this assumed that the T-sites were occupied by Si and Ga in a 2:1 ratio. The presence of a significant amount of Ga as an impurity means that this Si/Ga ratio may be greater than 2. However, if this Si/Ga ratio has become higher than 2, it has not got to the range where any leucite analogues are replaced by Ga-containing feldspar analogous to $RbAlSi_3O_8$ (Gasperin, 1971), which has a $C2/m$ monoclinic crystal structure.

To investigate the stoichiometry, specifically the Si/Ga ratio in this $RbGaSi_2O_6$ sample, SEM and EDS were used to analyze different areas of this sample.

EDS mapping was used to investigate the spatial distribution of the constituent elements of the sample qualitatively (see Figure 9). From these maps, it is evident that in regions where the gallium content is high, there is a drop in silicon content. This is therefore consistent with there being an increased volume fraction of Ga_2O_3 in this region. Further investigation of the sample revealed inclusions of Ga_2O_3 in the $RbGaSi_2O_6$ matrix (see Figure 10a,b). Theoretically, for a volume fraction of 12% Ga_2O_3 in a matrix of 88% $RbGaSi_2O_6$, where both components are stoichiometric, we would expect a composition of 31.23 wt.% O, 28.20 wt.% Ga, 24.47 wt.% Rb, and 16.08 wt.% Si. A wide area EDX spectrum was acquired from an approximate area of 1 mm^2; the averaged composition of this area is 32.5 wt.% O, 26.6 wt. % Ga, 22.7 wt.% Rb, and 18.2 wt.% Si. This is in close

agreement with the XRD result (see Figure 11a,b). Additionally, a point spectrum (see Figure 10c) in the $RbGaSi_2O_6$ matrix gives a composition of 29.3 wt.% O, 21.5 wt.% Ga, 27.1 wt.% Rb, and 22.1 wt.% Si. This would suggest that the $RbGaSi_2O_6$ matrix has a Si/Ga ratio close to 2.

Figure 4a,b (873 and 298 K; Bell and Stone, 2021), respectively, shows the VESTA crystal structure plots for $RbGaSi_2O_6$. Note that Figure 4b shows that the tetragonal crystal structure has a slightly collapsed silicate framework structure compared with the cubic structure shown in Figure 4a.
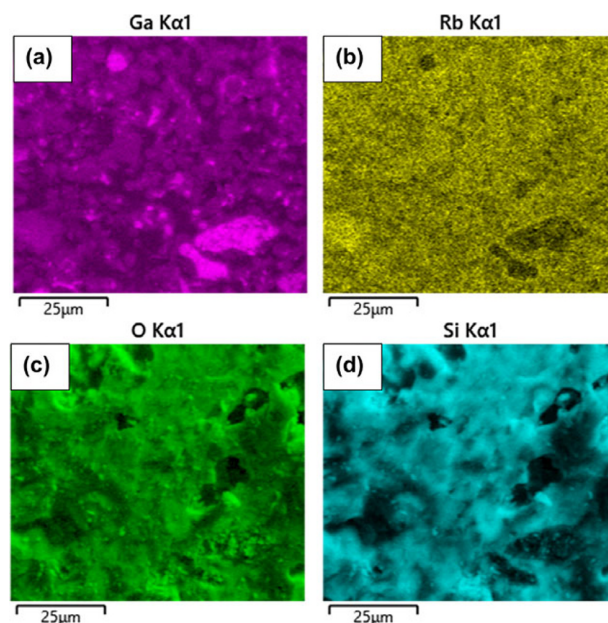

Figure 9. Qualitative EDX mapping of the $RbGaSi_2O_6$ sample: (a) gallium map; (b) rubidium map; (c) oxygen map; and (d) silicon map.
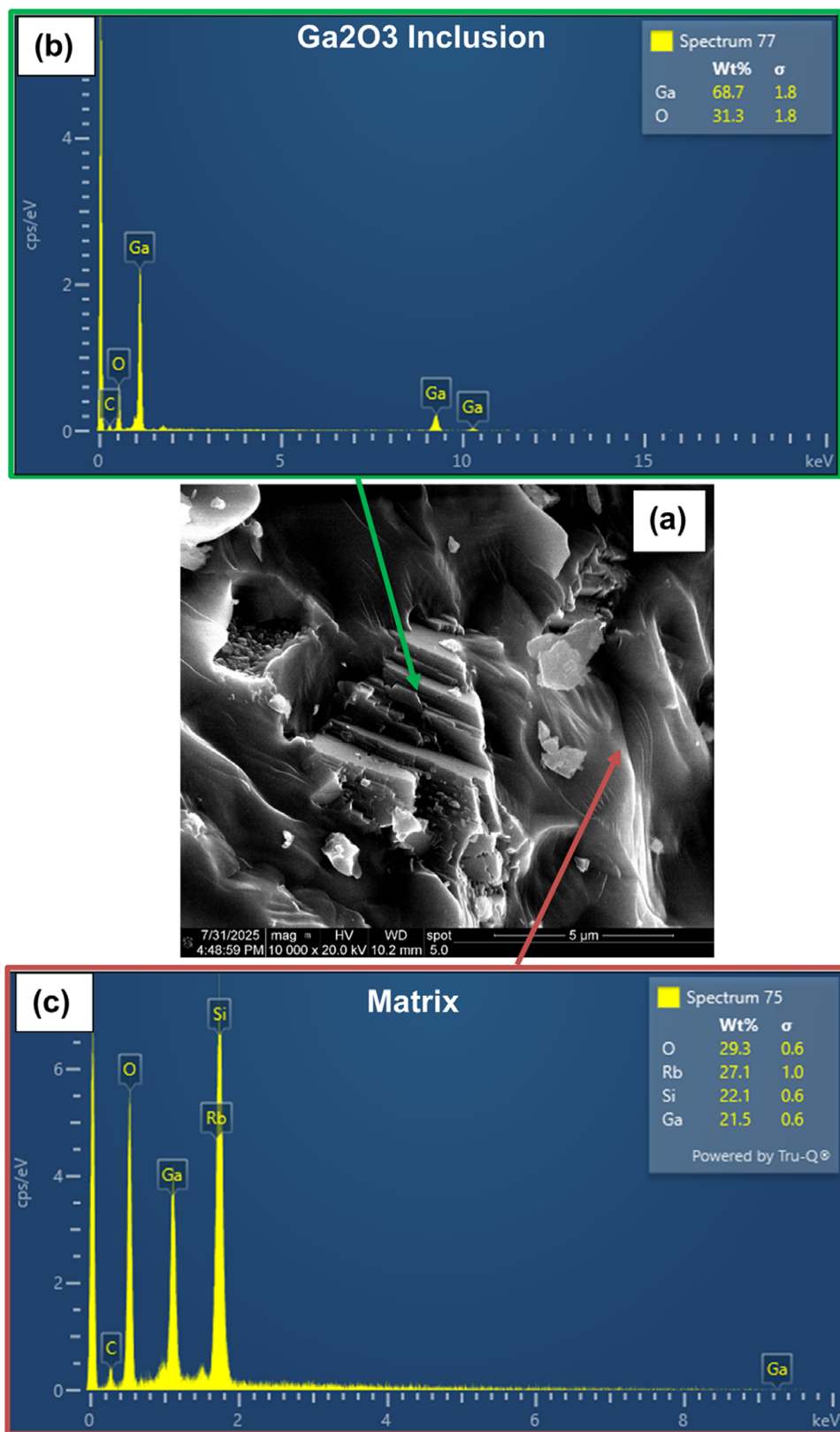
Figure 10. Scanning electron microscopy image of a Ga_2O_3 inclusion: (a) secondary electron image; (b) energy dispersive spectroscopy (EDS) spectrum obtained from a Ga_2O_3 inclusion; and (c) EDS spectrum recorded from the matrix.
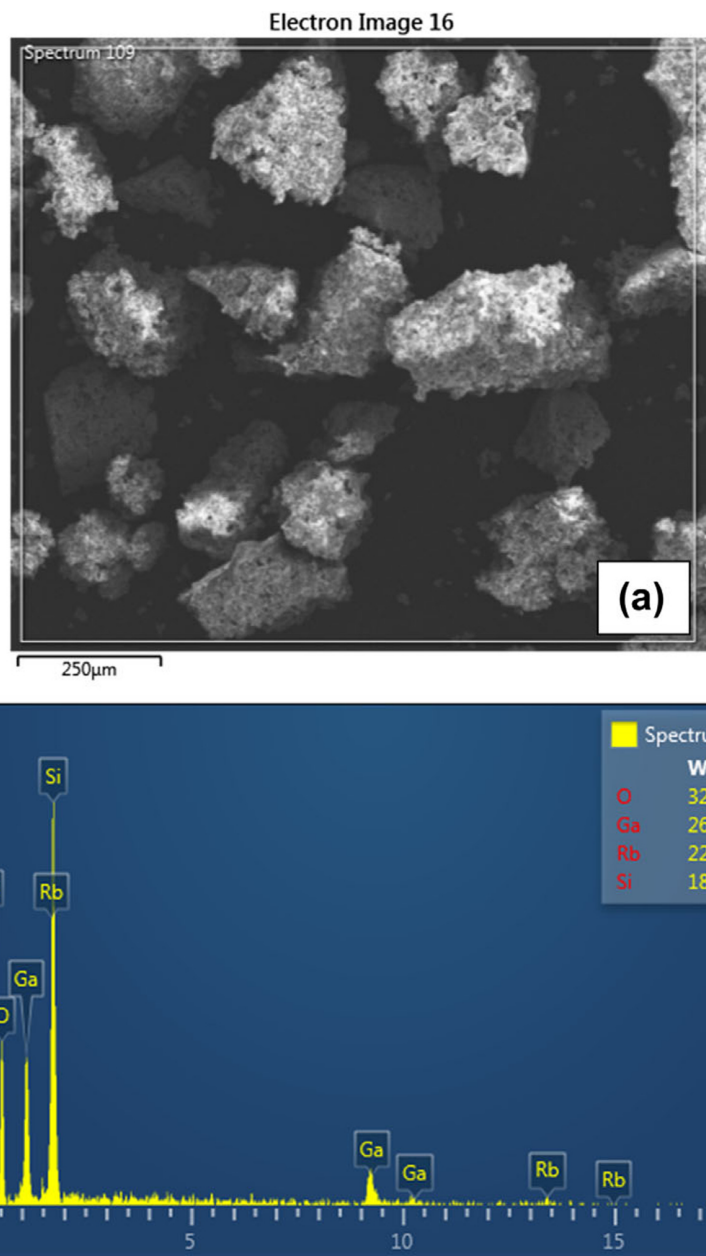
Figure 11. Scanning electron microscopy image acquired from an approximate area of 1 mm^2: (a) secondary electron image and (b) energy dispersive spectroscopy spectrum.

IV. CONCLUSIONS

RbGaSi$_2$O$_6$ leucite analogue has a high-temperature phase transition from $I4_1/a$ tetragonal (KAlSi$_2$O$_6$ leucite structure) to $Ia\overline{3}d$ cubic (CsAlSi$_2$O$_6$ pollucite structure) at 733 K. This transition is reversible on cooling to room temperature.

DEPOSITED DATA

CIF files containing information on the 873 K crystal structure, interatomic distances and angles, and powder diffraction data for RbGaSi$_2$O$_6$ synthetic leucite analogue were deposited with the ICDD. These data can be requested from ICDD at info@icdd.com.

REFERENCES

Bell, A. M. T. 2021. "Rietveld Refinement of the Low Temperature Crystal Structures of Cs$_2$XSi$_5$O$_{12}$ (X = Cu, Cd and Zn)." *European Journal of Chemistry* 12 (1): 60–63. https://doi.org/10.5155/eurjchem.12.1.60-63.2089.

Bell, A. M. T. 2023. "Orthorhombic-Cubic Phase Transition in Rb$_2$CoSi$_5$O$_{12}$ Leucite Analogue." *Minerals* 13 (2): 210. https://doi.org/10.3390/min13020210.

Bell, A. M. T. 2025. "Crystal Structures of Leucites – Past, Present, and Future?" *Crystallography Reviews*: 1–39. https://doi.org/10.1080/0889311X.2025.2553295.

Bell, A. M. T., F. Clegg, and C. M. B. Henderson. 2021. "Monoclinic-Orthorhombic First-Order Phase Transition in $K_2ZnSi_5O_{12}$ Leucite Analogue; Transition Mechanism and Spontaneous Strain Analysis." *Mineralogical Magazine* 85 (5): 752–71. https://doi.org/10.1180/mgm.2021.67.

Bell, A. M. T., and C. M. B. Henderson. 1994a. "Rietveld Refinement of Dry-Synthesized $Rb_2ZnSi_5O_{12}$ Leucite by Synchrotron X-Ray Powder Diffraction." *Acta Crystallographica* C50: 984–86. https://doi.org/10.1107/s0108270194002039.

Bell, A. M. T., and C. M. B. Henderson. 1994b. "Rietveld Refinement of the Structures of Dry-Synthesized M Fe(III) Si_2O_6 Leucites (M=K,Rb,Cs) by Synchrotron X-Ray Powder Diffraction." *Acta Crystallographica* C50: 1531–36. https://doi.org/10.1107/s0108270194004014.

Bell, A. M. T., and C. M. B. Henderson. 1996. "Rietveld Refinement of the Orthorhombic *Pbca* Structures of $Rb_2CdSi_5O_{12}$, $Cs_2MnSi_5O_{12}$, $Cs_2CoSi_5O_{12}$ and $Cs_2NiSi_5O_{12}$ Leucites by Synchrotron X-Ray Powder Diffraction." *Acta Crystallographica* C52: 2132–39. https://doi.org/10.1107/s0108270196003162.

Bell, A. M. T., and C. M. B. Henderson. 2009. "Crystal Structures and Cation Ordering in $Cs_2MgSi_5O_{12}$, $Rb_2MgSi_5O_{12}$ and $Cs_2ZnSi_5O_{12}$ Leucites." *Acta Crystallographica* B65: 435–44. https://doi.org/10.1107/s0108768109024860.

Bell, A. M. T., and C. M. B. Henderson. 2012. "High-Temperature Synchrotron X-Ray Powder Diffraction Study of $Cs_2XSi_5O_{12}$ (X = cd, cu, Zn) Leucites." *Mineralogical Magazine* 76 (5): 1257–80. https://doi.org/10.1180/minmag.2012.076.5.12.

Bell, A. M. T., and C. M. B. Henderson. 2016. "Rietveld Refinement of the Crystal Structures of $Rb_2XSi_5O_{12}$ (X = Ni, Mn)." *Acta Crystallographica* E72: 249–52. https://doi.org/10.1107/s2056989016001390.

Bell, A. M. T., and C. M. B. Henderson. 2018. "Crystal Structures of $K_2[XSi_5O_{12}]$ ($X = Fe^{2+}$, Co, Zn) and $Rb_2[XSi_5O_{12}]$ (X = Mn) Leucites: Comparison of Monoclinic $P2_1/c$ and $Ia\overline{3}d$ Polymorph Structures and Inverse Relationship between Tetrahedral Cation (T = Si and X)—O Bond Distances and Intertetrahedral T—O—T Angles." *Acta Crystallographica* B74: 274–86. https://doi.org/10.1107/s2052520618004092.

Bell, A. M. T., and C. M. B. Henderson. 2019. "A Study of Possible Extra-Framework Cation Ordering in *Pbca* Leucite Structures with Stoichiometry $RbCsX^{2+}Si_5O_{12}$ (X = Mg, Ni, Cd)." *Powder Diffraction* 34 (Supplement S1): S2–7. https://doi.org/10.1017/s0885715619000071.

Bell, A. M. T., and C. M. B. Henderson. 2020. "Tetragonal-Cubic Phase Transition in $KGaSi_2O_6$ Synthetic Leucite Analogue and its Probable Mechanism." *Journal of Solid State Chemistry* 284: 121142. https://doi.org/10.1016/j.jssc.2019.121142.

Bell, A. M. T., C. M. B. Henderson, S. A. T. Redfern, R. J. Cernik, P. E. Champness, A. N. Fitch, and S. C. Kohn. 1994a. "Structures of Synthetic $K_2MgSi_5O_{12}$ Leucites by Integrated X-Ray Powder Diffraction, Electron Diffraction and ^{29}Si MAS NMR Methods." *Acta Crystallographica* B50: 31–41. https://doi.org/10.1107/s0108768193008754.

Bell, A. M. T., K. S. Knight, C. M. B. Henderson, and A. N. Fitch. 2010. "Revision of the Structure of $Cs_2CuSi_5O_{12}$ Leucite as Orthorhombic *Pbca*." *Acta Crystallographica* B66: 51–59. https://doi.org/10.1107/s0108768109054895.

Bell, A. M. T., S. A. T. Redfern, C. M. B. Henderson, and S. C. Kohn. 1994. "Structural Relations and Tetrahedral Ordering Pattern of Synthetic Orthorhombic $Cs_2CdSi_5O_{12}$ Leucite: A Combined Synchrotron X-Ray Powder Diffraction and Multinuclear MAS NMR Study." *Acta Crystallographica* B50: 560–66. https://doi.org/10.1107/S0108768194003393

Bell, A. M. T., and A. H. Stone. 2021. "Crystal Structures and X-Ray Powder Diffraction Data for $Cs_2NiSi_5O_{12}$, $RbGaSi_2O_6$ and $CsGaSi_2O_6$ Synthetic Leucite Analogues." *Powder Diffraction* 36 (4): 273–81. https://doi.org/10.1017/S0885715621000580.

Carpenter, M. A., E. K. H. Salje, and A. Graeme-Barber. 1998. "Spontaneous Strain as a Determinant of Thermodynamic Properties for Phase Transitions in Minerals." *European Journal of Mineralogy* 10 (4): 621–91.

da Silva, M. A. F. M., L. P. Sosman, F. Yokaichiya, V. L. Mazzocchi, C. B. R. Parente, J. Mestnik-Filho, P. F. Henry, and H. N. Bordallo. 2012. "Neutron Powder Diffraction Measurements of the Spinel $MgGa_2O_4$: Cr^{3+}: A Comparative Study between the High Flux Diffractometer D2B

at the ILL and the High Resolution Powder Diffractometer Aurora at IPEN." *Journal of Physics: Conference Series* 340: 1–7.

Finger, L. W., D. E. Cox, and A. P. Jephcoat. 1994. "A Correction for Powder Diffraction Peak Asymmetry Due to Axial Divergence." *Journal of Applied Crystallography* 27: 892–900. https://doi.org/10.1107/S0021889894004218.

Gasperin, M. 1971. "Structure Cristalline de $RbAlSi_3O_8$." *Acta Crystallographica* B27: 854–55. https://doi.org/10.1107/S0567740871003078.

Gatta, G. D., N. Rotiroti, M. Fisch, M. Kadiyski, and T. Armbruster. 2008. "Stability at High-Pressure, Elastic Behaviour and Pressure-Induced Structural Evolution of $CsAlSi_5O_{12}$, a Potential Host for Nuclear Waste." *Phys. Chem. Minerals* 35: 521–33. https://doi.org/10.1007/s00269-008-0246-2.

Kabekkodu, S., A. Dosen, and T. N. Blanton. 2024. "PDF-5+: A Comprehensive Powder Diffraction File™ for Materials Characterization." *Powder Diffraction* 39: 47–59. https://doi.org/10.1017/S0885715624000150.

Mazzi, F., E. Galli, and G. Gottardi. 1976. "The Crystal Structure of Tetragonal Leucite." *American Mineralogist* 61: 108–15.

Momma, K., and F. Izumi. 2011. "VESTA 3 for Three-Dimensional Visualization of Crystal, Volumetric and Morphology Data." *Journal of Applied Crystallography* 44: 1272–76. https://doi.org/10.1107/S0021889811038970.

Palmer, D. C., M. T. Dove, R. M. Ibberson, and B. M. Powell. 1997. "Structural Behavior, Crystal Chemistry, and Phase Transitions in Substituted Leucite: High-Resolution Neutron Powder Diffraction Studies." *American Mineralogist* 82: 16–29. https://doi.org/10.2138/am-1997-1-203.

PANalytical. 2017a. *Data Collector 5.5a (Computer Software)*. Almelo: PANalytical.

PANalytical. 2017b. *High Score Plus 4.7 (Computer Software)*. Almelo: PANalytical.

Redfern, S. A. T., and C. M. B. Henderson. 1996. "Monoclinic-Orthorhombic Phase Transition in the $K_2MgSi_5O_{12}$ Leucite Analog." *American Mineralogist* 81: 369–74. https://doi.org/10.2138/am-1996-3-411.

Rietveld, H. M. 1969. "A Profile Refinement Method for Nuclear and Magnetic Structures." *Journal of Applied Crystallography* 2: 65–71. https://doi.org/10.1107/S0021889869006558.

Rodríguez-Carvajal, J. 1993. "Recent Advances in Magnetic Structure Determination by Neutron Powder Diffraction." *Physica B* 192: 55–69. https://doi.org/10.1016/0921-4526(93)90108-I.

Robinson, K., G. V. Gibbs, and P. H. Ribbe. 1971. "Quadratic Elongation: A Quantitative Measure of Distortion in Coordination Polyhedra." *Science* 172: 567–70. https://doi.org/10.1126/science.172.3983.567.

Taylor, D., and C. M. B. Henderson. 1968. "The Thermal Expansion of the Leucite Group of Minerals." *American Mineralogist* 53: 1476–88.

Toby, B. H., and R. B. Von Dreele. 2013. "GSAS-II: The Genesis of a Modern Open-Source all Purpose Crystallography Software Package"." *Journal of Applied Crystallography* 46 (2): 544–49. https://doi.org/10.1107/S0021889813003531.

Torres-Martinez, L. M., and A. R. West. 1984. "Synthesis of $Rb_2BeSi_5O_{12}$ with a Leucite Structure." *Journal of Materials Science Letters* 3: 1093–94. https://doi.org/10.1007/BF00719774.

Torres-Martinez, L. M., and A. R. West. 1986. "New Family of Silicate Phases with the Pollucite Structure." *Zeitschrift für Kristallographie* 175: 1–7. https://doi.org/10.1524/zkri.1986.175.1-2.1.

Torres-Martinez, L. M., and A. R. West. 1989. "Pollucite- and Leucite-Related Phases: $A_2BX_5O_{12}$ and ACX_2O_6 (A = K, Rb, Cs; B = Be, Mg, Fe, Co, Ni, Cu, Zn, Cd; C = B, Al, Ga, Fe, Cr; X = Si)." *Zeitschrift für anorganische und allgemeine Chemie* 578: 223–30. https://doi.org/10.1002/zaac.19895730123.

Torres-Martinez, L. M., J. A. Gard, R. A. Howie, and A. R. West. 1984. "Synthesis of $Cs_2BeSi_5O_{12}$ with a Pollucite Structure." *Journal of Solid State Chemistry* 51: 100–3. https://doi.org/10.1016/0022-4596(84)90320-7.

van Laar, B., and W. B. Yelon. 1984. "The Peak in Neutron Powder Diffraction." *Journal of Applied Crystallography* 17: 47–54. https://doi.org/10.1107/S0021889884011006.

Yanase, I., H. Kobayashi, Y. Shibasaki, and T. Mitamura. 1997. "Tetragonal-to-Cubic Structural Phase Transition in Pollucite by Low-Temperature X-Ray Powder Diffraction." *Journal of the American Ceramic Society* 80: 2693–95. https://doi.org/10.1111/j.1151-2916.1997.tb03175.x.